Title

Modular soft x-ray spectrometer for applications in energy sciences and quantum materials

Journal

Review of Scientific Instruments, 88(1)

ISSN

0034-6748

Authors

Chuang, Yi-De

Shao, Yu-Cheng

Cruz, Alejandro

et al.

Publication Date

2017

DOI

10.1063/1.4974356

Peer reviewed

Modular soft x-ray spectrometer for applications in energy sciences and quantum materials

Yi-De Chuang, Yu-Cheng Shao, Alejandro Cruz, Kelly Hanzel, Adam Brown, Alex Frano, Ruimin Qiao, Brian Smith, Edward Domning, Shih-Wen Huang, L. Andrew Wray, Wei-Sheng Lee, Zhi-Xun Shen, Thomas P. Devereaux, Jaw-Wern Chiou, Way-Faung Pong, Valeriy V. Yashchuk, Eric Gullikson, Ruben Reininger, Wanli Yang, Jinghua Guo, Robert Duarte, and Zahid Hussain

Citation: Rev. Sci. Instrum. **88**, 013110 (2017); doi: 10.1063/1.4974356

View online: http://dx.doi.org/10.1063/1.4974356

View Table of Contents: http://aip.scitation.org/toc/rsi/88/1

Published by the American Institute of Physics

Modular soft x-ray spectrometer for applications in energy sciences and quantum materials

Yi-De Chuang,[1,a)] Yu-Cheng Shao,[2] Alejandro Cruz,[1] Kelly Hanzel,[3] Adam Brown,[3] Alex Frano,[1,4] Ruimin Qiao,[1] Brian Smith,[3] Edward Domning,[3] Shih-Wen Huang,[5] L. Andrew Wray,[6] Wei-Sheng Lee,[7] Zhi-Xun Shen,[7,8] Thomas P. Devereaux,[7] Jaw-Wern Chiou,[9] Way-Faung Pong,[2] Valeriy V. Yashchuk,[1] Eric Gullikson,[10] Ruben Reininger,[11] Wanli Yang,[1] Jinghua Guo,[1] Robert Duarte,[3] and Zahid Hussain[1]

[1]*Advanced Light Source, Lawrence Berkeley National Laboratory, Berkeley, California 94720, USA*
[2]*Department of Physics, Tamkang University, New Taipei City 25137, Taiwan*
[3]*Engineering Division, Lawrence Berkeley National Laboratory, Berkeley, California 94720, USA*
[4]*Department of Physics, University of California, Berkeley, California 94720, USA*
[5]*MAX IV Laboratory, Lund University, SE221-00 Lund, Sweden*
[6]*Department of Physics, New York University, New York, New York 10003, USA*
[7]*Stanford Institute for Materials and Energy Sciences, SLAC National Accelerator Laboratory, Menlo Park, California 94025, USA*
[8]*Department of Physics, Stanford University, Stanford, California 94305, USA*
[9]*Department of Applied Physics, National University of Kaohsiung, Kaohsiung 811, Taiwan*
[10]*Center for X-ray Optics, Lawrence Berkeley National Laboratory, Berkeley, California 94720, USA*
[11]*Advanced Photon Source, Argonne National Laboratory, Argonne, Illinois 60439, USA*

(Received 12 October 2016; accepted 8 January 2017; published online 27 January 2017)

Over the past decade, the advances in grating-based soft X-ray spectrometers have revolutionized the soft X-ray spectroscopies in materials research. However, these novel spectrometers are mostly dedicated designs, which cannot be easily adopted for applications with diverging demands. Here we present a versatile spectrometer design concept based on the Hettrick-Underwood optical scheme that uses modular mechanical components. The spectrometer's optics chamber can be used with gratings operated in either inside or outside orders, and the detector assembly can be reconfigured accordingly. The spectrometer can be designed to have high spectral resolution, exceeding 10 000 resolving power when using small source (~1 μm) and detector pixels (~5 μm) with high line density gratings (~3000 lines/mm), or high throughput at moderate resolution. We report two such spectrometers with slightly different design goals and optical parameters in this paper. We show that the spectrometer with high throughput and large energy window is particularly useful for studying the sustainable energy materials. We demonstrate that the extensive resonant inelastic X-ray scattering (RIXS) map of battery cathode material $LiNi_{1/3}Co_{1/3}Mn_{1/3}O_2$ can be produced in few hours using such a spectrometer. Unlike analyzing only a handful of RIXS spectra taken at selected excitation photon energies across the elemental absorption edges to determine various spectral features like the localized *dd* excitations and non-resonant fluorescence emissions, these features can be easily identified in the RIXS maps. Studying such RIXS maps could reveal novel transition metal redox in battery compounds that are sometimes hard to be unambiguously identified in X-ray absorption and emission spectra. We propose that this modular spectrometer design can serve as the platform for further customization to meet specific scientific demands.
[http://dx.doi.org/10.1063/1.4974356]

I. INTRODUCTION

When electrons in a material are excited by X-rays, the system can return to its ground state by re-emitting photons and electrons. Measuring the energy and momentum of emitted photons and electrons, thereby using energy and momentum conservations to deduce a material's response to the excitation photon field, has been one of the most direct ways to study the electronic structure of the material.[1,2] Although soft X-ray spectroscopies based on measuring photons, such as X-ray Emission Spectroscopy (XES), Resonant Inelastic X-ray Scattering spectroscopy (RIXS), and X-ray Absorption Spectroscopy (XAS) with fluorescence yield detection, are known to have much smaller cross-sections compared to the ones based on measuring electrons, unlike the electron spectroscopies, these photon spectroscopies can be used in the presence of electric and/or magnetic fields. With elemental, chemical, and bonding selectivity and bulk sensitivity, they are the ideal techniques for *in situ* and *in operando* studies.[3–6]

[a)]Author to whom correspondence should be addressed. Electronic mail: ychuang@lbl.gov

The key instrument for spectroscopic inelastic probes like XES and RIXS is the soft X-ray spectrometer for analyzing the energy of the emitted photons (in combination with a suitable beamline). In the soft X-ray regime (below ~2 keV), reflection gratings are commonly used for this purpose. In fact, grating-based soft X-ray spectrometers (referred to as spectrometers hereafter) will out-perform other types of photon analyzers, like superconducting tunneling junction (STJ),[7,8] transition edge sensor (TES),[9] and silicon drift detector (SDD),[10,11] in terms of attainable energy resolution.

Over the past decade, the rapid development of spectrometers has revolutionized the soft X-ray spectroscopies in a wide range of scientific fields. This is particularly true for RIXS: active research using this technique to study various excitations in strongly correlated materials manifesting emergent quantum phenomena has offered new perspective to condensed matter physics.[6,12–16] With advanced grating manufacturing technology, varied line spacing (VLS) gratings ruled on spherical or plane substrates are commonly used in these spectrometers. Different optical schemes besides the Rowland circle geometry are explored: based on the success of prior high resolution spectrometers,[17–19] some are pursuing the ultrahigh energy resolution by using very long spectrometers (with dedicated beamlines to deliver ~μm beam on the sample) coupled to horizontal collimating mirrors to enlarge the angular acceptance;[20,21] some are aiming for high throughput by making the spectrometers compact[22–26] or utilizing multiple orders of gratings to record soft X-rays emitted from various elements in the sample simultaneously.[27] Some schemes even use the energy compensation[28] or cross-dispersion[29] concepts to take advantage of the off-axis radiation that is blocked by the beamline exit slit to enhance the throughput or gain the incident photon energy dependence information without loss of energy resolution. Besides the reflection gratings, some spectrometers use ultrahigh line density transmission gratings to improve the throughput.[30,31] These advanced spectrometers, whether having an astounding 15 m length to achieve ultrahigh energy resolution, or being very compact to have ultrahigh throughput, are designed with their respective mechanical novelties. Their opto-mechanical designs are optimized for dedicated beamlines. What we propose here is different: a compact, portable, and modular slitless spectrometer design for a wide range of applications.

An attempt to produce a general purpose, compact spectrometer to serve the larger soft X-ray spectroscopy community was initiated more than a decade ago by a commercial company (VG Scienta) using the design of a constant line-spacing, spherical grating spectrometer (GRACE, Rowland circle geometry) from Nordgren *et al.*[32] This spectrometer, XES 350, has a fixed opto-mechanical design with resolving power (RP, E/ΔE) up to 2000 when a 10 μm source is used. Although an entrance slit can be used as the virtual source when working with a large real source to preserve the RP, using the entrance slit leads to severe reduction in the vertical acceptance angle, which affects the throughput of spectrometer. This aspect is well-recognized in free electron laser (FEL) and bioscience research where enlarging X-ray beam spot on the sample is often used in experiments to mitigate the sample radiation damage issue.

In the process of developing a soft X-ray spectrometer for both synchrotron and FEL applications, we took the approach of modularizing the key components of a spectrometer such that its mechanism can be reconfigured to work with different types of gratings (plane or spherical figure) at either inside or outside diffraction order, as well as with various source (e.g., from ~5 μm to ~25 μm in the current design) and detector pixel resolutions (effectively 27 μm in the commercial CCD or spectroCCD, see later discussion). This approach better capitalizes the engineering effort invested in the mechanical design when reconfiguration is needed. In addition, standardizing the spectrometer components allows the vendors to stockpile items, such as grating substrates that have very long lead-time and components that are costly when manufactured with small quantity, to expedite the production and lower the unit cost. The modular spectrometer can also serve as the platform for further customization for specific scientific demands. This paper reports two slightly different Hettrick-Underwood type soft X-ray spectrometer designs using the modular mechanical components: one with grating operated in the inside order for working with a large source and small pixel detector (modular X-ray spectrometer or MXS, see Section II) and the other with gratings operated in the outside order for working with a small source and the commercial CCD detector (see Section IV).

The paper is structured as follows: in Section II, we present the opto-mechanical design of MXS for a momentum-resolved RIXS endstation (qRIXS, see Figure 1 for the CAD model). In Section III, we show the preliminary XES and RIXS data from battery cathode materials measured at BL8.0.1 of the Advanced Light Source (ALS), Lawrence Berkeley National Laboratory (LBNL), using MXS installed in another endstation called *in situ* RIXS (*i*RIXS), which will be described elsewhere. The spectrometer's high throughput enables the generation of extensive RIXS maps within few hours of measurement time. By analyzing the RIXS maps, we show that the obtained information can facilitate the energy research at the ALS. In Section IV, we present the variation of MXS for another project with distinct source parameters and performance requirements. Although the detector assembly is quite

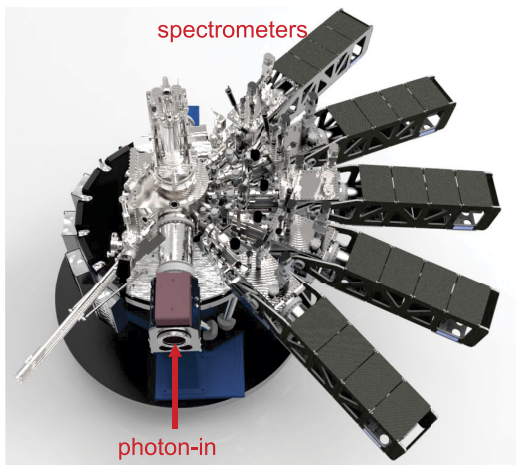

FIG. 1. CAD model of qRIXS endstation with five modular soft X-ray spectrometers (MXS) on top of the experimental platform.

different, the variant uses nearly identical optical chamber (U-bracket is changed for different mirror angle, see Section II A) as MXS. In Section V, we give the conclusions and outlook of this project.

II. DESIGN OF MODULAR SOFT X-RAY SPECTROMETER (MXS)

A. Optical design

We hope to develop an endstation that can be used to perform both static and time-resolved, momentum-resolved resonant inelastic X-ray scattering spectroscopy. The static measurements will be performed at the ALS, while the time-resolved measurements will be performed at FEL facilities, such as Linac Coherent Light Source (LCLS) at SLAC National Accelerator Laboratory. For momentum-resolved RIXS spectroscopy, the spectrometer needs to be moved in the scattering plane relative to the incident photon beam so that the photon momentum transfer to the sample, $\Delta\vec{q} = \vec{k}_o - \vec{k}_i$, can be varied (changing $\vec{k}_o$ while fixing $\vec{k}_i$). Here, $\vec{k}_i$ and $\vec{k}_o$ are the momentum of incident and emitted photons, respectively. Because qRIXS will be moved in between facilities, the entire endstation needs to be mobile. This requirement rules out the option of putting spectrometers inside the experimental chamber, as the system will become too cumbersome for transportation. It also prohibits the use of a sliding face seal at the interface between experimental chamber and spectrometers: there will be limited space to put the spectrometer optics, and implementing such sliding seal requires an integral design of the experimental chamber with beamlines.

Based on our pervious experience, we decided to use up to five standalone spectrometers mounted to the emission ports on the experimental chamber that sits on top of a rotatable platform.[23,33] These spectrometers have to be supported from the endstation platform, instead of from the floor underneath them. In that regard, the Hettrick-Underwood optical scheme with much simpler detector motion is chosen so that a lighter detector assembly can be constructed to reduce the cantilever load.[34,35]

There are two optical elements in the Hettrick-Underwood optical scheme (see Figure 2(a) for the schematic plot): a spherical mirror for focusing the emitted X-rays from the sample onto the imaging detector, and the VLS plane grating for dispersing photons with different energies, imaging the virtual source created by the spherical mirror at the detector, and correcting the aberrations of both optical elements. The VLS terms can be chosen to optimize the energy resolution over a photon energy range, or at one photon energy but correcting multiple high order aberrations. In the current design, we choose the VLS terms such that high order aberrations up to spherical aberration (F_{40} term) are corrected at 640 eV (Mn L_3 edge). As will be shown later, the Hettrick-Underwood optical scheme also gives the relatively good flat field imaging capability ideal for the energy materials research.

There are other considerations in the optical design. The spectrometer is required to have moderate energy resolution (maximum 5000 resolving power at 540 eV) to match that of the monochromator of soft X-ray beamline (SXR) at LCLS.[36] In the meantime, it also needs to have high throughput to accommodate the reduced photon flux density, which is essential to avoid the non-linear effect induced by the extremely intense X-rays from such a low repetition rate source when the beam spot on the sample is small. Limited by the available space around the experimental floor, the length of the spectrometer cannot exceed 2.2 m. The interior of the experimental chamber needs to be large enough to house refocusing mirrors for the THz pump laser (off-axis parabola). In addition, two isolation valves and a vacuum transition section are needed in between the experimental chamber and spectrometers so that when moving the spectrometers from port to port, both the experimental chamber and spectrometers can stay under the vacuum. These factors limit how close the spherical mirror can be placed relative to the sample, which should be at least 0.7 m from our practical experience.

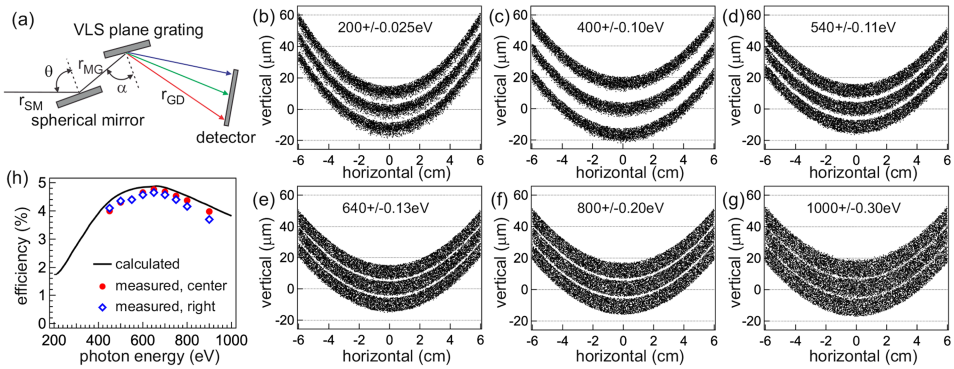

FIG. 2. (a) Schematic illustration of Hettirck-Underwood optical scheme. ((b)-(g)) SHADOW simulations showing the scattered dot images at the detector plane at selected photon energies: (b) 200 eV, (c) 400 eV, (d) 540 eV, (e) 640 eV, (f) 800 eV, and (g) 1000 eV. In each panel, three photon energies (one central and two detuned) are used to show the energy resolution. The amount of energy detuning is listed in each panel. (h) The calculated (black line) and measured (markers) grating efficiency curves. The red filled circles and blue open diamonds denote the efficiencies from the central and right (viewing from upstream) grating stripes on the substrate.

Since this spectrometer (named MXS) is designed to work with X-rays from FEL where a large beam spot (e.g., 25 μm or larger vertically) will be used to mitigate sample radiation damage issue, we plan to use an R&D CCD detector that has 5 μm pixel spatial resolution to achieve the moderate RP (spectroCCD, with 5 μm (v) × 45 μm (h) rectangular pixels; details of this spectroCCD will be described elsewhere). Alternatively, we can use the KBr-coated small pore microchannel plates with CMOS based detector (timepix) to achieve ~7 μm spatial resolution after centroiding.[37,38] Thus in the optical design, the source and detector pixel sizes are set to 25 μm (along the dispersion direction of spectrometer grating; the other dimension can be up to 1 mm in size) and 7 μm, respectively. The source and detector pixel contributed resolutions are balanced at 640 eV, and the grating will be operated in inside order (+1). One should note that when working with a smaller source, such as ~10 μm that is available at synchrotron beamlines, the resolution of MXS will be limited by the detector pixel size even with these novel detectors. For now, we will use a commercial CCD detector (ANDOR, DO936) in MXS until the aforementioned novel detectors are properly packaged to work with the spectrometer.

The following parameters are used in the optical design: r_{SM} = 0.9 m, r_{MG} = 0.1 m, and r_{GD} ~ 1.1 m (this distance will depend on photon energy), R = 29.472 m, θ = 88°, and α = 88.5°. Here, r_{SM}, r_{MG}, r_{GD} are the sample-to-mirror, mirror-to-grating, and grating-to-detector distances. R is the radius of the spherical mirror and θ is its incidence angle. α is the incidence angle of the grating (see Figure 2(a)). The spectrometer grating will be operated in (nearly) constant incidence angle mode (see Section II D 2). The maximum angular acceptance is 2.6 mrad (v) × 60 mrad ((h), see later discussion). We follow the approach by Amemiya *et al.*[39,40] to determine the VLS terms. The calculated VLS terms g_0 (constant), g_1 (linear), g_2 (quadratic), and g_3 (cubic) are (in SHADOW[41,42] convention): g_0 = 24 000 l/cm, g_1 = 435.259 l/cm^2, g_2 = 5.757 l/cm^3, and g_3 = 0.07 l/cm^4. The local groove density $g(\omega)$ can be calculated using the equation: $g(\omega) = g_0 + g_1 \times \omega + g_2 \times \omega^2 + g_3 \times \omega^3$, where ω is the (signed) tangential position of grooves relative to the grating pole. With these VLS parameters, the focal length r_{GD} will change by about 6 mm from 1100.7 mm (1000 eV) to 1094.3 mm (200 eV). Thus, a linear translation stage will be required to move the detector along the optical path to stay in focus.

B. SHADOW ray-tracing results

Figures 2(b)–2(g) show the SHADOW ray-tracing results with the aforementioned parameters at selected photon energies. In the simulations, the source is a 25 μm (v) × 100 μm (h) rectangle. The beam divergence is 2.6 mrad (v) × 60 mrad (h), matching the clear apertures of spherical mirror and VLS plane grating. The slope error contributions to energy resolution are negligible and are not included in the simulations. Each panel shows the scattered dot image at the detector plane normal to the optical path, which is produced by propagating photons with three different energies (one central and two detuned energies; energy detuning is listed in each panel) through the spectrometer. From these figures, one can see that this optical design will give moderate RP around 5000 at 640 eV. RP decreases with increasing photon energy, and it drops down to ~3000 at 1 keV. At high photon energy, the resolution will be limited by the source size, thus RP can be slightly improved by reducing the source size (close down the beamline slits). Although RP increases rapidly with decreasing photon energy, as can be seen in Figures 2(b) and 2(c), one should note that after correcting the aberrations, the resolution will be limited by the detector pixel size.

C. Grating efficiency

To increase the spectrometer throughput, we plan to stack multiple (3 for the current optical design) spectroCCD sensors side-by-side to enlarge the horizontal acceptance angle up to 60 mrad. To take advantage of this wide detector, the clear apertures of spherical mirror and VLS plane grating are set to 80 mm (l) × 80 mm (w) and 90 mm (l) × 80 mm (w), respectively. The mirror and grating substrates have dimensions of 90 mm (l) × 90 mm (w) and 100 mm (l) × 90 mm (w) so that there are 5 mm gaps all around the clear apertures. The spherical mirror and plane grating substrates are manufactured by Carl Zeiss GmbH and InSync, Inc., respectively. The measured slope error of the mirror is 0.3 μrad (RMS), and it is better than 0.2 μrad for the grating substrates. Instead of having a very wide grating that will have wrong groove spacing $g(\omega)$ around the edges, there are three identical grating stripes on a substrate, with each stripe having the dimension of 80 mm (l) × 20 mm (w) and 3 mm gaps in between the stripes. X-rays reflected off these gaps (un-ruled area) will have different emission angles (β, $\beta = 2\theta - \alpha$ and is positive in this convention) compared to the ones reflected off the gratings. They will be blocked by the beam masks (see later discussion), producing dark stripes on the CCD. These dark stripes can be used to place the source position relative to the center of the grating stripe.

These gratings are etched directly into the silicon substrate and coated with Au by Shimadzu Corp. They have laminar groove profiles with 35% land width and 6.5 nm groove depth to optimize the efficiency around 640 eV. The grating efficiency is calculated using GSolver® and measured at BL6.3.2 at the ALS. The calculated (black line) and measured (markers) efficiencies are shown in Figure 2(h). The calculation shows that due to the use of high line density, the maximum efficiency is slightly less than 5% around 640 eV. The central stripe (red filled circles) has measured efficiency better than 90% of the theoretical value, suggesting its high groove fidelity. Although the side stripe (blue open diamonds) has slightly lower efficiency, presumably due to a slightly different groove profile, it still has >80% of the theoretical efficiency. So for practical applications, all stripes can be used with comparable efficiencies.

D. Mechanical design

The CAD model of MXS is shown in Figure 3(a). It comprises three major components: optics chamber, detector assembly, and mounting mechanism.

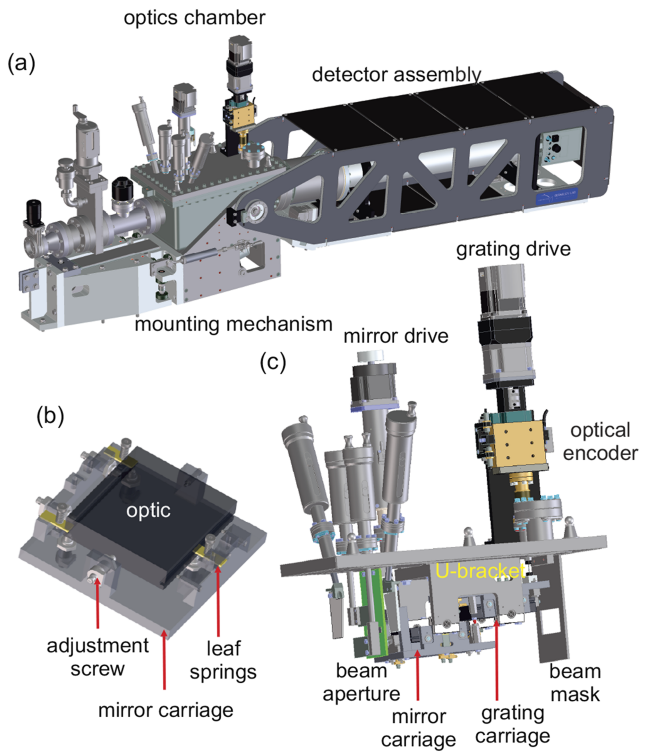

FIG. 3. CAD models showing (a) an overview of MXS, which comprises three major components: optics chamber, detector assembly, and mounting mechanism, (b) the optics carriage, and (c) the interior view of the optics chamber.

1. Optics chamber

The optics chamber is compact so that multiple spectrometers can be placed close to each other (see Figure 1). Nevertheless, the mechanical design gives enough interior room to hold moderate size optics. The dimension of the optics chamber is 16.40 in. (L) × 10.00 in. (W) × 7.50 in. (H) (not including the motion feedthroughs). The maximum size of the optics that can be installed in the current design is 90 mm (W) × 100 mm (L). The interior of the optics chamber is shown in Figure 3(c). We use the flange-mount design for housing the optics: mirror and grating assemblies are attached to a rectangular stainless steel-aluminum bimetal base flange. Both mirror and grating substrates are captured inside their own Al carriages (see Figure 3(b)). The substrates have two side grooves, allowing them to be held down by three BeCu leaf springs against the 1/4-100 spring-loaded adjustment screws in the back side (Siskiyou, 100TPI-0.2H-VC, also see Figure 7(b)). Three spring plungers (Vlier, SSS52) and same 1/4-100 adjustment screws are also used to secure the substrates horizontally. This method of grabbing optics against the counter force springs ensures that no net force can be transmitted to the optical surface to distort the surface figures.

The mirror and grating carriages are attached to a U-shape bracket via flex pivots (Riverhawk, 5016-600). This U-bracket can be machined precisely so that the distance between the centers of flex pivots is exactly 10 cm. If one wishes to change the mirror incidence angle θ and/or r_{MG}, one only needs to replace this U-bracket and adjust the length of wire linkage accordingly (see Section IV). The U-bracket is then attached to the bimetal base flange. Since the entire assembly is very compact, the positions of the optics relative to the centers of the flex pivots can be adjusted by turning the 1/4-100 adjustment screws under the survey of coordinate measurement machine (CMM). The whole optics chamber can then be fiducialized using CMM to achieve the precision better than 5 μm and installed to the endstation and beamline with fiducial information [there are four fiducial monuments on the rectangular base flange for recording the fiducial information].

The mirror and grating angles can be changed by the motorized linear feedthrough and linear translation stage, respectively. This degree of freedom offers the opportunity for users to partly compensate errors such as wrong VLS parameters and alignment error during the beam-based optimization without breaking the vacuum of the spectrometer. For the three MXS installed in qRIXS, we use stepper motors with integrated control boards (IMS, MDI3CRL23B7-EE, and MDI3CRL17A4-EE) [NEMA 23 motors are used for mirror drive, grating drive, and the detector rotation, whereas NEMA 17 motor is used for detector translation]. For the MXS installed in *i*RIXS, they are regular stepper motors (Parker, HV232-01-FL and HV173-01-FL).

For the mirror drive mechanism, a wire linkage is used to attach the mirror carriage to the linear feedthrough. The mirror carriage is pre-loaded against the pulling force; thus by pulling this wire linkage, the mirror angle can be changed. The motion of wire linkage is recorded by an absolute optical encoder (MicroE, M3000-M10-200-1; 0.1 μm resolution) with glass scale (MicroE, L30) all mounted inside the linear feedthrough. The translation is converted to the mirror angular rotation using CMM, and the converted step resolution is 1.7 μrad per encoder count.

The same wire linkage concept is also used in the grating carriage. For better stability, a linear translation stage is used instead (ALM, MLP3-3-1). The translation of this stage is recorded by an optical encoder (Renishaw, RGH24Y-50F-33A; 0.1 μm resolution) with optical tape scale (Renishaw, RGS-20S) and a magnetic reference mark mounted on the side of the stage. The converted step resolution for grating rotation is also 1.7 μrad per encoder count. Since the stepper motor is coupled to the linear translation stage through a 10:1 gearhead (Parker, PX23-010-S2), the stability of grating angle is better than 1.7 μrad.

A set of blades forming the four-jaw aperture is placed before the spherical mirror. Each blade can be independently adjusted (manual or motorized) by the linear feedthroughs (VacGen, ZLDS950 and ZLDS925). The aperture will not only be used to define the illumination on optics during normal operation, but can also be used to find the center of optics in the initial alignment and commissioning process. Additional beam masks are installed before the spherical mirror and after the VLS grating to further minimize the scattered X-rays off the optical path that can be accidentally reflected into the detector. There are additional mounting holes inside the spectrometer fly tube between the grating and detector. If needed, more beam defining masks can be installed using these mounting holes. All internal components and the rectangular optics chamber are made out of Al (except the blades that are made out of OFHC copper) for their lightweight. The optics chamber is sealed using Al wires for UHV compatibility.

2. Detector assembly

A commercial CCD detector (ANDOR, DO936-BN) is currently mounted at the end of spectrometer fly tube, which is connected to the optics chamber via an 8 in. bellow. This big bellow allows the detector to be rotated about the pivot point close to the grating pole, and translated along the optical path to fulfill the focusing condition. The detector translation is achieved by using two sets of linear guides (THK, HRW21CA1UU), one master and one slave, at both ends of the fly tube. This motion, which is 25 mm in the current design, is motorized so that the detector translation can be synchronized with photon energy scan. To overcome the vacuum and bellow forces, a miniature gearhead (Harmonic, CSF-11-30-2XH-J) is used for the NEMA 17 motor on the master guide assembly. The detector position is recorded by the Renishaw RGH24Y optical encoder, same as the one used in the grating drive stage, with tape scale and magnetic reference mark.

The detector and its drive mechanism are captured by a pair of carbon fiber arms. Carbon fiber is chosen for its exceptional mechanical rigidity and lightweight, and the fibers are laid in such a way that the coefficient of thermal expansion (CTE) is minimized. The detector assembly is driven by a motorized jacking screw underneath the optics chamber, which gives the rotational motion needed when measuring X-rays with different photon energies (see Figure 2(a) for the schematic plot). A 10:1 gearhead (Parker, PX23-010-S2) is used for the NEMA 23 motor on the jacking screw. The angular rotation is recorded by an optical encoder assembly (Renishaw, RGH20O50F33A and RESR20USA075) mounted on the rotational axis. In this configuration, the total angular range for detector rotation is 12.1°, with step resolution of 0.27 μrad per encoder count. During the commissioning, we observed the long-term angular stability better than 5 encoder counts (1.4 μrad). This stability is acceptable considering the relatively short acquisition time with ANDOR detector. All motorized motions are protected by the high precision mechanical limit switches (Baumer, Mycom F100/80).

With the mechanism shown in Figure 3, the detector position (or r_{GD}), as well as the detector and grating angles (hence α and β angles), can all be changed independently. One can show that by varying α slightly from the designed angle (88° in this case) and searching for the global minimum of the vector sum of coma F_{30} and spherical aberration F_{40} with r_{GD} satisfying the focusing F_{20} term, the aberrations can be significantly reduced. This approach, called coma-free operation and is commonly used for the spherical VLS grating spectrometers, can also be realized in our spectrometer design.[43]

3. Support mechanism

The spectrometer will be supported off the top experimental platform using a six-point kinematic mount that consists of six flat and round (20 in. radius) surfaces. These kinematic contacts are made out of hardened stainless steel. This mounting mechanism is designed specifically for the spectrometers in qRIXS endstation, and it will depend on the applications. In general, if the spectrometer does not have to be moved, the support can be built directly on the floor to enhance the stability.

III. PERFORMANCE OF MODULAR SOFT X-RAY SPECTROMETER (MXS)

A. Straight beam test

We use a synchrotron beam straight through a pinhole to test the energy resolution of MXS at BL6.3.2 at the ALS. The test configuration is shown in Figures 4(a) and 4(b). A 25 μm pinhole is mounted at the end of a sample stick, which is attached to the manipulator so that the pinhole can be moved around the photon beam to maximize the transmission. The spectrometer is aligned to the beamline using fiducial information. Because the synchrotron beam is highly collimated compared to the divergent X-rays emitted from the sample, only a small region around the center of the optics will be illuminated. With such small footprints ($\omega \sim 0$), the aberrations will become negligible. Thus the straight beam test can only be used to validate the best performance of the spectrometer.

The test is performed around 500 eV with beamline resolving power (E/ΔE) set around 3000, and the results are shown in Figure 4(c). The markers represent the integrated intensity on CCD across the non-dispersive direction (horizontal direction in this design), and the red and blue lines are Gaussian fittings. Two photon energies are shown in this figure: 500 eV (red filled circles) and 501 eV (blue open squares). The FWHM of the peak is 0.3 eV, suggesting that RP is around 1600. This RP is roughly a factor of 4 smaller than the designed value. Although ANDOR DO936-BN has 13.5 μm square physical pixels, the large point spread function (PSF) gives the effective ~27 μm pixels.[17] Thus the spectrometer RP is expected to be reduced by a factor of 4 (~27/7) owing to the lower

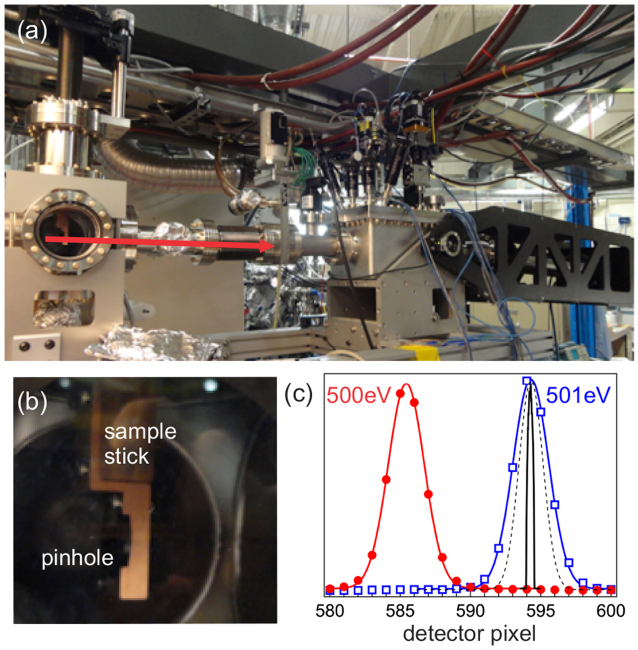

FIG. 4. (a) Photograph showing the setup of straight beam test at BL6.3.2 at the ALS. The red arrow indicates the beam path. (b) Zoom-in view of the interior of the pinhole chamber, where pinhole is attached to the end of a sample stick. (c) Test results at 500 eV and 501 eV photon energies. The markers are the data from CCD and red and blue lines are the Gaussian fittings. The thick black line shows the simulated beam profile from a 25 μm circular pinhole, and the thin dashed black line shows the effect of broadening by the detector point spread function (see text).

spatial resolution of CCD pixels. This is illustrated by the thin dashed line in this figure, which is the convolution of the thick black line (simulated histogram of the beam from a 25 μm circular pinhole at 501 eV) and a Gaussian function with 27 μm FWHM representing the contribution from the detector PSF. The discrepancy in the peak widths is due to finite beamline resolution, which is not considered in the simulation.

B. Preliminary XES and RIXS measurements

One of the four MXSs built at the ALS thus far is currently installed in the *in situ* RIXS (*i*RIXS) endstation at BL8.0.1 at the ALS. The details of the *i*RIXS endstation will be described elsewhere.[44] *i*RIXS is developed with focuses on studying materials for sustainable energy applications; therefore, having high detection efficiency and a wide photon energy window is essential for the spectrometer to perform *in situ* and *in operando* measurements.

One of the main research topics at *i*RIXS is the energy storage (battery) materials, which is the core of electric vehicles and grid scale electricity storage.[45] Among all modern battery technologies, lithium-ion battery remains to be the system-of-choice in terms of energy density, ever since the first generation $LiCoO_2$/graphite based batteries were commercialized in the 1990s. One of the technical challenges for Li-ion batteries is the development of positive electrode materials with safe, low-cost, and high-capacity performance.[46] Extensive efforts based on soft X-ray absorption spectroscopy have been invested to study the battery electrode materials under both *ex situ*[3,47,48] and *in situ*[49,50] conditions. Replacing Co in $LiCoO_2$ with other elements while retaining the layer structure, e.g., forming materials like $LiNi_{0.8}Co_{0.15}Al_{0.05}O_2$ and $LiNi_{1/3}Co_{1/3}Mn_{1/3}O_2$, to improve the performance and reduce the material cost has been one of the promising approaches in both academic and industrial research and developments.[46,51] Additionally, $LiNi_{1/3}Co_{1/3}Mn_{1/3}O_2$ represents a typical multi-element system for soft X-ray spectroscopy. Therefore, we show the experimental XES and RIXS data from $LiNi_{1/3}Co_{1/3}Mn_{1/3}O_2$ in Figure 5 to showcase the potential of utilizing MXS for studying energy materials.

Figure 5(a) shows the non-resonant XES spectra collected in 1 min (red line) and 5 min (black line) at 900 eV excitation photon energy. Although the spectrum recorded in 5 min has sufficient statistics for detailed lineshape analysis, the one recorded in just 1 min is enough for identifying gross spectral features. The wide energy window of the spectrometer allows the features at O K, Mn $L_{2,3}$, Co $L_{2,3}$, and Ni $L_{2,3}$ edges to be recorded simultaneously. Additionally, due to the high detection efficiency, the much weaker $L_{2,3} - M_1$ decay channels[52] of Mn, Co, and Ni (in energy ranges marked by black horizontal bars) can also be observed. Such high efficiency and wide energy window of MXS spectrometer provide the most ever efficient probe of the valence band electronic structure with elemental and orbital sensitivities.

Figure 5(b) shows the RIXS map with excitation photon energies scanned through the Mn $L_{2,3}$ absorption edges.

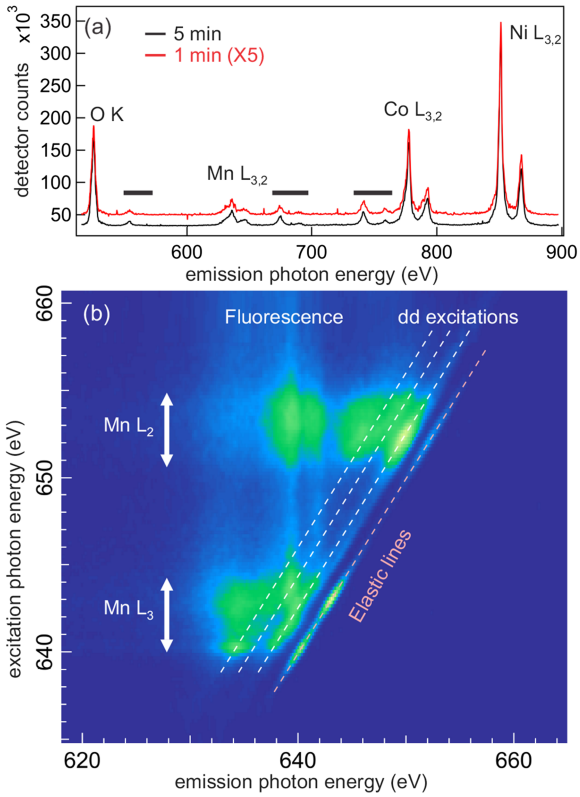

FIG. 5. (a) XES spectra of $LiNi_{1/3}Co_{1/3}Mn_{1/3}O_2$ taken at 900 eV excitation photon energy with 300 (black) and 60 s (red, magnified by a factor of 5) measurement time. (b) RIXS map with excitation photon energy scanned through Mn $L_{2,3}$ edges. The elastic line and localized *dd* excitations are marked by pink and white dashed lines, respectively. The vertical broad lines are the non-resonant fluorescence features.

The energy resolution for this measurement is 0.5 eV. Using commercial XES 350 to record one RIXS spectrum can often take about 30 to 60 min, but the high efficiency of the MXS spectrometer reduces this time down to minutes. Thus producing such finely spaced, 0.2 eV energy step in this case, full energy range RIXS mapping takes about 4 h. The benefit of RIXS mapping compared to selected RIXS spectra at few photon energies is evident. In the case of Mn $L_{2,3}$ edge RIXS spectroscopy, one can see that the RIXS spectra from simple reference MnO[53] already exhibit the admixture of different types of emissions over the 10 eV energy loss window, let alone the spectra from materials such as $Li(Ni,Co,Mn)O_2$ that are expected to be more complicated. Figure 5(b) demonstrates the reliable extraction of multiple *dd* excitation modes (excitations associated with inter 3*d* orbital transitions): the energy distribution of the emitted photons associated with the core-level excitations is defined by the well resolved localized *dd* RIXS features (white dashed lines; parallel to the elastic line denoted by the pink dashed line) and non-resonant fluorescence features (vertical broad features). As the *dd* excitations are highly sensitive to the oxidation states of 3*d* transition metal elements,[2] such high-efficiency RIXS mapping could reveal novel transition metal redox in battery compounds that are sometimes unclear in typical XAS experiments (due to the large core-hole lifetime broadening).

IV. MODULAR SOFT X-RAY SPECTROMETER FOR OUTSIDE ORDER OPTICAL DESIGN

A. Optical design

As mentioned earlier, this modular X-ray spectrometer MXS can also be used with gratings operated in outside order (−1). One example is the spectrometer we developed for a beamline at Taiwan Photon Source (TPS), which has a pair of highly demagnifying Kirkpatrick-Baez (KB) mirrors to deliver a tightly focused beam (2 μm vertically, with 10 μm beamline exit slit setting) onto the sample. The spectrometer will be used in energy materials research, and is required to have a wider operating photon energy window from 250 eV to 1000 eV. The spectrometer's resolving power should be higher than 3000 over this energy window, and it should be optimized around 285 eV (C *K* edge) and 640 eV (Mn *L* edge). One should use commercially available CCD detectors in the spectrometer for day 1 experiments; however, the design reserves the option for future upgrade to advanced detectors with smaller pixels to improve the resolving power. Since a commercial ANDOR DO936-BN CCD detector will be used in this spectrometer, to balance the source and detector pixel contributed resolutions, the gratings will need to be operated in outside order. The spectrometer will be used in energy materials research, so having the nearly flat field imaging capability like MXS is highly desirable. In that regard, the Hettrick-Underwood optical scheme is also selected for this case.

Two gratings are used to cover a wide photon energy range: low energy grating (LEG, 250 eV to 700 eV) and high energy grating (HEG, 500 eV to 1000 eV). Both gratings will be operated in constant included angle (2θ), instead of constant incidence angle (α) mode, for lower horizon energies. 2θ is set to 174° to balance the throughput, e.g., the combination of optics reflectivity and the vertical acceptance angle, and RP. The optical design balances the energy resolutions from a 5 μm source and 13.5 μm detector pixels at 420 eV for LEG (see later discussion). The source size in this design is larger than what can be delivered by the beamline. The choice is made such that there is room for future upgrade with a small pixel imaging detector, where swapping out the current ANDOR CCD with new detector will automatically improve the energy resolution.

To accommodate the difference in the incidence angle of the spherical mirror (θ is changed from 88° to 87°) without invoking extensive redesign of the optics chamber, the grating pivot is vertically shifted by 3.509 mm. This increases r_{MG} by 0.306 mm. We keep the spectrometer length to be shorter than 3 m to maximizing the throughput with moderate RP. With these considerations, the following parameters are used in optical design: r_{SM} = 1.25 m, r_{MG} = 0.100 306 m, r_{GD} ~ 1.2 m (this distance will depend on photon energy), R = 24.355 m, and θ = 87°. The maximum angular acceptance is 3.4 mrad (v) × 26 mrad (h) for each ruling. Again, we follow the approach by Amemiya *et al.* to determine the VLS terms that optimize the spectrometer resolution at 420 eV. For LEG, they are g_0 = 9000 l/cm, g_1 = 149.746 l/cm^2, g_2 = 2.0058 l/cm^3, and g_3 = −0.008 l/cm^4. As for HEG, the central line density is scaled up by a factor of 2 while the ratios between VLS terms remain unchanged. Hence the VLS terms for HEG are g_0 = 18 000 l/cm, g_1 = 299.492 l/cm^2, g_2 = 4.0016 l/cm^3, and g_3 = −0.016 l/cm^4. The scaling of line density shifts the coverage energy range by the same factor.

B. SHADOW ray-tracing results

Figures 6(a)–6(e) show the SHADOW ray-tracing results with the aforementioned optical parameters for LEG at selected photon energies. The results for HEG will be the same, except the energies and energy resolutions are scaled up by a factor of 2. Hence HEG has the same RP at LEG at scaled photon energies without considering the slope error contributions. In the simulations, a 5 μm (v) × 100 μm (h) rectangular beam is used as the source. The beam divergence is 3.4 mrad (v) × 10 mrad (h), matching the length of clear aperture of spherical mirror and the width of ANDOR CCD detector. However, the footprint on the grating will be narrower than the 35 mm ruled width. The slope errors (0.32 μrad and 0.15 μrad for spherical mirror and plane grating substrates, respectively) are not included in the simulations, but they are expected to become noticeable with future upgrade with small pixel detector. Each panel shows the scattered dot image at the detector plane normal to the optical path.

From Figure 6(c), one can see that the designed RP for LEG at 420 eV will exceed 6000. This RP increases rapidly as

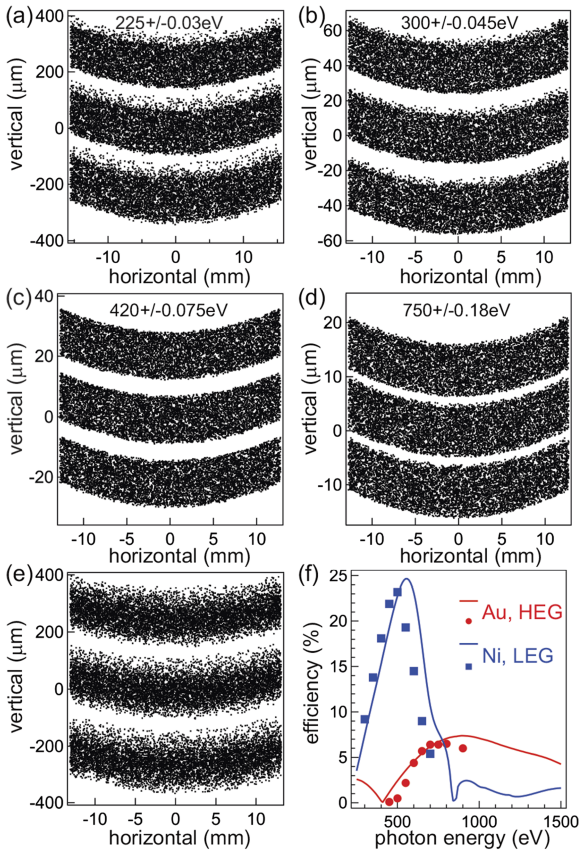

FIG. 6. ((a)-(e)) SHADOW simulations showing the scattered dot images at the detector plane at selected photon energies: (a) 225 eV, (b) 300 eV, (c) 420 eV, and (d) 750 eV. In each panel, three photon energies (one central and two detuned) are used to show the energy resolution. Panel (e) is the result at 225 eV, same as panel (a), except r_{GD} is kept at 1.275 m. (h) The calculated (lines) and measured (markers) grating efficiency curves. The red and blue curves are for Au coated HEG and Ni coated LEG, respectively.

photon energy decreases, and at 300 eV (Figure 6(b)), it can even approach 10 000. One should note that below 420 eV, the spectrometer resolution is limited by the source size. Thus during the normal operation, RP can be further improved by closing down the beamline slits. On the other hand, RP decreases as the photon energy increases. The spectrometer resolution above 420 eV will be limited by the detector pixel size, as can be seen from the effective vertical width of the image that is smaller than the 13.5 μm pixel size (for example, see Figure 6(d)). So in the case of 750 eV, the actual RP will be lower than 4000.

To achieve the best energy resolution, the detector position needs to be varied with respect to photon energy to stay in focus. This can be accomplished by using a linear translation stage to move the detector along the optical path. For energies above 300 eV for LEG (or 600 eV for HEG), r_{GD} remains around 1.2 m. r_{GD} increases rapidly as photon energy decreases: r_{GD} becomes 1.255 m at 255 eV and 1.77 m at 225 eV. In order for the detector to stay in focus at low photon energies, a very large translation stage will be needed to provide such long travel. However, the spectrometer has considerable depth of focus that RP is somewhat preserved even if the detector is not in focus. This is demonstrated in Figure 6(e) where we repeat the same simulation as that in Figure 6(a), except r_{GD} is kept to 1.275 m. Although the images do not show a sharp edge as those in Figure 6(a), the spectrometer RP is still preserved. This large depth of focus permits the use of a smaller translation stage for detector motion and greatly simplifies the mechanical design of the detector assembly.

C. Grating efficiency

Like MXS, the spherical mirror and plane grating substrates are manufactured by Carl Zeiss GmbH and InSync, Inc., respectively, and the gratings are ruled by Shimadzu Corp. The clear apertures of spherical mirror and grating substrates remain to be 80 mm (l) × 80 mm (w) and 90 mm (l) × 80 mm (w), respectively. But unlike MXS where there are three identical gratings on a single substrate, this spectrometer has two different gratings ruled on a single substrate (also see Figure 7(b)). Each ruling has the dimension of 80 mm (l) × 35 mm (w) and a 4 mm gap in between the rulings. The LEG is coated with Ni to have higher efficiency at low photon energy. It has the laminar groove profile with 30% land width and 10 nm groove depth to optimize the efficiency around 540 eV. The HEG is coated with Au and has the laminar groove profile with 40% land width and 6 nm groove depth to optimize the efficiency around 850 eV. The calculated (lines) and measured (markers) efficiencies are shown in Figure 6(f). The blue and red curves/markers are results from LEG and HEG, respectively.

Ni coating gives LEG a very high efficiency, up to 23%, at 500 eV. However, the measured efficiency deviates significantly from the calculated one, presumably due to the absorption of the surface oxide layer. This efficiency drops below 5% above 700 eV and shows Ni absorptions around 850 eV. On the low energy side, at 300 eV, the efficiency remains around 10%, which is sufficient for carbon-based materials research.

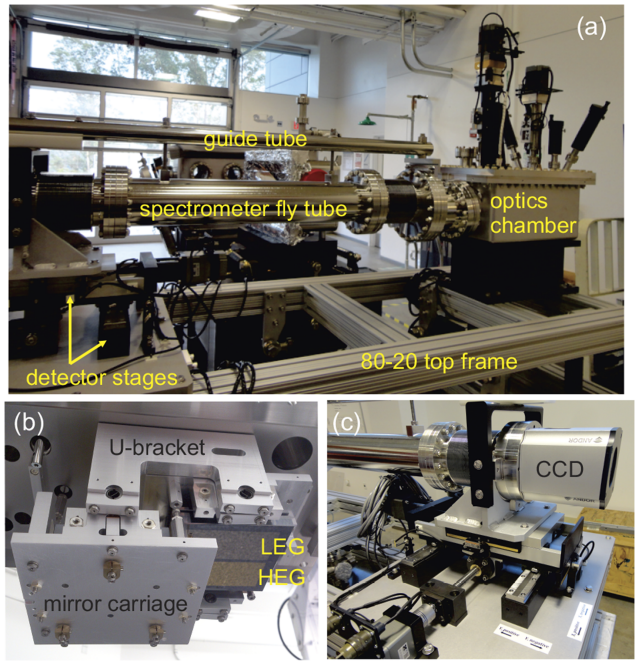

FIG. 7. Photographs showing (a) the spectrometer developed for a beamline at Taiwan Photon Source, (b) the internal construction of the optics chamber with Ni coated LEG and Au coated HEG, and (c) the detector assembly.

For HEG, the grating efficiency approaches 0 around 400 eV due to horizon energy. The efficiency increases monotonically with photon energy and reaches ~7% around 800 eV. Although limited by the measurement that we do not have data points above 1000 eV, the comparison between calculated and measured efficiencies suggests that the grating can still be usable up to 1500 eV. We notice that there is a crossover between the efficiencies of LEG and HEG around 700 eV. In addition, based on SHADOW simulations in Figures 6(a)–6(d), RP of LEG decreases rapidly around this energy. Therefore for practical applications, we expect the users will use HEG above 700 eV to have better efficiency and energy resolution.

D. Mechanical design

The optics chamber is nearly identical to MXS for qRIXS and iRIXS endstations. Since the grating pivot is vertically shifted by 3.509 mm relative to the mirror pivot, the only components inside the vacuum chamber that are modified are the U-bracket and beam mask after the grating (see Figure 3(c)). In the airside, the stepper motors are changed (OrientalMotor, PKE569AC) to be compatible with the control system at TPS beamline.

The detector assembly is shown in Figure 7(a). The ANDOR DO936-BN CCD detector is mounted on an XY platform (see Figure 7(c)) formed by a linear translation stage (ALM, 11742-01-SPA, set at 80 mm travel range) and two transverse linear rails (THK, HRW21CA2UUC1+320L). A spectrometer fly tube is connected to the optics chamber and detector via two bellows. This fly tube is suspended from a guide tube, which has the pivot point at the upstream coupling flange and two slots to allow the suspension studs to slide along the length of the tube. The detector can be translated

along and across the beam path to stay in focus and detect the X-rays diffracted from different gratings (see Figure 7(b)). The translational degrees of freedom are motorized using stepper motors (OrientalMotor, PKE564AC-HS100) so that the detector motion can be synchronized with photon energy scans. The translations are recorded using Renishaw RGH24 optical encoders, with tape scales and magnetic reference marks like the ones on the grating drive mechanism. The mechanical limit switches (Omeron, D5A-3210) are also used for motion protection.

The spectrometer is supported by an 80-20 top frame, which is connected to the 80-20 base frame using six-struts (see Figure 7(a)). Since the spectrometer will be fixed at 90° emission geometry, the 80-20 frame is designed to have lower profile for better rigidity and stability. The space between the experimental floor and the bottom frame will be filled with granite blocks to provide a stable platform.

E. Straight beam test

Without a suitable beamline and endstation to commission the spectrometer with X-rays emitted from the sample, we resort to the straight beam test. As discussed earlier, this test can only validate the best performance of the spectrometer, if its RP is lower than that of the beamline. The test is performed at BL8.0.1 at the ALS with a similar setup shown in Figure 4(a). In the test, a 5 μm pinhole mounted on the sample stick serves as the virtual source. The detector is translated side ways to collect X-rays diffracted from LEG (test is done on LEG only). Figure 8(a) shows the binned spectra on CCD at selected photon energies. To measure different photon energies, the grating needs to be rotated towards the spherical mirror. This changes α and β angles and brings the images back to the detector. Unlike MXS, the CCD detector does not move in the vertical plane.

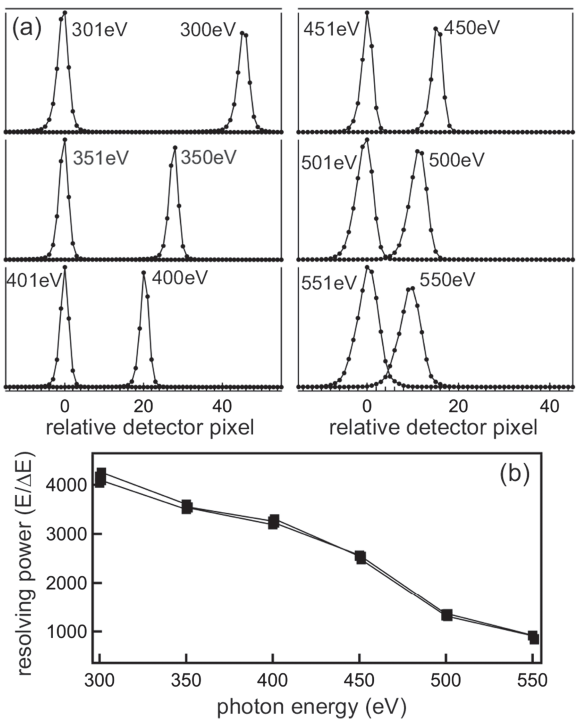

FIG. 8. (a) Straight beam test results at selected photon energies for LEG. (b) Resolving power of spectrometer as a function of photon energy determined from the Gaussian fittings to the curves in panel (a). Two sets of curves correspond to two repeated measurements.

Because the 5 μm pinhole is placed further downstream from the focus of an upstream vertical focusing mirror (beam spot is ~4 orders of magnitude larger than the pinhole size at pinhole location), to have sufficient flux for the test, the beamline slits are opened up to 60 μm (entrance slit) × 60 μm (exit slit). With this large slit setting, the beamline RP is around 4000 at 300 eV and it drops down to <2000 at 500 eV (with medium energy grating in the beamline monochromator). From Figure 8(b), one can see that the spectrometer has reasonably good RP at low photon energy, reaching 4000 at 300 eV. However, RP decreases monotonically with increasing photon energy and drops below 1000 above 550 eV. Compared to the simulations in Figure 6, it is clear that the measured RP is at least a factor of 2 lower than the simulated one. The reduced RP is not due to the larger pinhole in use, as the inspection of pinhole under microscope confirms its 5 μm size. The 27 μm effective detector pixel is also considered in calculating the theoretical RP. The lower RP is in fact contributed by the beamline resolution with large slit setting. Or equivalently, this spectrometer has higher RP than beamline under this test condition. We expect that with this spectrometer installed at the beamline at TPS, proper commission can be performed to validate its performance.

V. CONCLUSIONS AND OUTLOOK

We have developed a modular soft X-ray spectrometer design based on the Hettrick-Underwood optical scheme. We have constructed 5 spectrometers, four identical ones (called MXS) for applications at the ALS and LCLS, and a variant that will be used at TPS beamline. MXS has three identical grating rulings on one substrate, which will be operated in inside order; whereas for the TPS spectrometer, there are two different grating rulings (LEG and HEG) on one substrate that will be operated in outside order. Furthermore, MXS works with larger source spot (25 μm in design) while the variant works with a small source spot (5 μm in design). Although these spectrometers had slightly different design goals and optical parameters, they were all built using nearly identical components. Their performances were tested using a straight synchrotron beam through the respective pinhole, but the resolving power was limited by the detector pixel resolution (for MXS) or beamline resolution. The preliminary XES and RIXS results from battery cathode material $LiNi_{1/3}Co_{1/3}Mn_{1/3}O_2$ using the high efficiency MXS showcase its potential in producing the full energy range RIXS maps. This kind of RIXS maps, encompassing rich information about the electronic structure and elementary excitations, can facilitate the materials research with X-ray spectroscopies.

The versatile mechanical design of MXS makes it an ideal platform for further customization for specific science needs. For example, it can be used with spherical VLS grating where one optical element performs both focusing and energy monochromatization. For that, one simply removes the

spherical mirror assembly (carriage and drive mechanism) from the optics mount and adjusts the entrance and exit ports on the Al chamber accordingly. The spectrometer can also be designed to be very compact for high throughput partial fluorescence yield detection, as the optics can be placed very close to the sample if allowed by the acceptable energy resolution, aberration, clear apertures, and mechanical mounting mechanisms. Such compact spectrometer will have performance that rivals the SDD in terms of energy resolution, but much simpler to operate and user friendly. Although the current mechanical design does not have the capability to switch the gratings, this can be easily incorporated by using in-vacuum translation stage with in-vacuum piezo motors.

ACKNOWLEDGMENTS

The Advanced Light Source is supported by the Director, Office of Science, Office of Basic Energy Sciences, of the U.S. Department of Energy under Contract No. DE-AC02-05CH11231. W.-S.L, Z.-X.S. and T.P.S. are supported by the U. S. Department of Energy, Office of Science, Basic Energy Sciences, Materials Sciences and Engineering Division, under Contract DE-AC02-76SF00515. The Advanced Photon Source is supported by the Director, Office of Science, Office of Basic Energy Sciences, of the U.S. Department of Energy under Contract No. DE-AC02-06CH11357. qRIXS endstation and MXS are partially funded by Department of Energy, Office of Science, Basic Energy Sciences, Materials Sciences and Engineering Division, under Contract DE-AC02-76SF00515.

[1] P. Kuiper, J.-H. Guo, C. Såthe, L.-C. Duda, J. Nordgren, J. J. M. Pothuizen, F. M. F. de Groot, and G. A. Sawatzky, Phys. Rev. Lett. **80**, 5204 (1998).
[2] F. de Groot and A. Kotani, *Core Level Spectroscopy of Solids* (CRC Press, 2008).
[3] W. Yang, X. Liu, R. Qiao, P. Olalde-Velasco, J. D. Spear, L. Roseguo, J. Pepper, Y.-D. Chuang, J. D. Denlinger, and Z. Hussain, J. Electron Spectrosc. Relat. Phenom. **190**, 64 (2013).
[4] X. Liu, W. Yang, and Z. Liu, Adv. Mater. **26**, 7710 (2014).
[5] Y.-S. Liu, P.-A. Glans, C.-H. Chuang, M. Kapilashrami, and J.-H. Guo, J. Electron Spectrosc. Relat. Phenom. **200**, 282 (2015).
[6] L. J. P. Ament, M. van Veenendaal, T. P. Devereaux, J. P. Hill, and J. van den Brink, Rev. Mod. Phys. **83**, 705 (2011).
[7] S. Friedrich, C. A. Mears, B. Nideröst, L. J. Hiller, M. Frank, S. E. Labov, A. T. Barfknecht, and S. P. Cramer, Microsc. Microanal. **4**, 616 (1999).
[8] S. Friedrich, M. H. Carpenter, O. B. Drury, W. K. Warburton, J. Harris, J. Hall, and R. Cantor, J. Low Temp. Phys. **167**, 741 (2012).
[9] J. N. Ullom and D. A. Bennett, Supercond. Sci. Technol. **28**, 084003 (2015).
[10] G. Bertuccio, M. Sampietro, and A. Fazzi, Nucl. Instrum. Methods Phys. Res., Sect. A **322**, 538 (1992).
[11] P. Lechner, A. Pahlke, and H. Soltau, X-Ray Spectrom. **33**, 256 (2004).
[12] J. Nordgren and J.-H. Guo, J. Electron Spectrosc. Relat. Phenom. **110**, 1 (2000).
[13] A. Kotani and S. Shin, Rev. Mod. Phys. **73**, 203 (2001).
[14] W. Schülke, *Electron Dynamics by Inelastic X-Ray Scattering* (Oxford Press, 2007).
[15] M. Simon and T. Schmitt, J. Electron. Spectrosc. Relat. Phenom. **188**, 1 (2013).
[16] T. Schmitt, F. M. F. de Groot, and J.-E. Rubensson, J. Synchrotron Radiat. **21**, 1065 (2014).
[17] G. Ghiringhelli, A. Piazzalunga, C. Dallera, G. Trezzi, L. Braicovich, T. Schmitt, N. V. Strocov, R. Betemps, L. Patthey, X. Wang, and M. Grioni, Rev. Sci. Instrum. **77**, 113108 (2006).
[18] N. V. Strocov, T. Schmitt, U. U. Flechsig, T. Schmidt, A. Imhof, Q. Chen, J. Raabe, R. Betemps, D. Zimoch, J. Krempasky, X. Wang, M. Grioni, A. Piazzalunga, and L. Patthey, J. Synchrotron Radiat. **17**, 631 (2010).
[19] Y. Harada, M. Kobayashi, H. Niwa, Y. Senba, H. Ohashi, T. Tokushima, Y. Horikawa, S. Shin, and M. Oshima, Rev. Sci. Instrum. **83**, 013116 (2012).
[20] N. B. Brookes *et al.* http://www.esrf.eu/home/UsersAndScience/Experiments/EMD/ID32/RIXS.html.
[21] J. Dvorak, I. Jarrige, V. Bisogni, S. Coburn, and W. Leonhardt, Rev. Sci. Instrum. **87**, 115109 (2016).
[22] C. F. Hague, J. H. Underwood, A. Avila, R. Delaunay, H. Ringuenet, M. Marsi, and M. Sacchi, Rev. Sci. Instrum. **76**, 023110 (2005).
[23] Y.-D. Chuang, J. Pepper, W. McKinney, Z. Hussain, E. Gullikson, P. Batson, D. Qian, and M. Z. Hasan, J. Phys. Chem. Solids **66**, 2173 (2006).
[24] M. Agåker, J. Andersson, C.-J. Englund, A. Olsson, M. Ström, and J. Nordgren, Nucl. Instrum. Methods Phys. Res., Sect. A **601**, 213 (2009).
[25] S. G. Chiuzbăian, C. F. Hague, A. Avila, R. Delaunay, N. Jaouen, M. Sacchi, F. Polack, M. Thomasset, B. Lagarde, A. Nicolaou, S. Brignolo, C. Baumier, J. Lüning, and J.-M. Mariot, Rev. Sci. Instrum. **85**, 043108 (2014).
[26] Z. Yin, H. B. Peters, U. Hahn, M. Agåker, A. Hage, R. Reininger, F. Siewert, J. Nordgren, J. Viefhaus, and S. Techert, Rev. Sci. Instrum. **86**, 093109 (2015).
[27] O. Fuchs, L. Weinhardt, M. Blum, M. Weigand, E. Umbach, M. Bär, C. Heske, J. Denlinger, Y.-D. Chuang, W. McKinney, Z. Hussain, E. Gullikson, M. Jones, P. Batson, B. Nelles, and R. Follath, Rev. Sci. Instrum. **80**, 063103 (2009).
[28] C. H. Lai, H. S. Fung, W. B. Wu, H. Y. Huang, H. W. Fu, S. W. Lin, S. W. Huang, C. C. Chiu, D. J. Wang, L. J. Huang, T. C. Tseng, S. C. Chung, C. T. Chen, and D. J. Huang, J. Synchrotron Radiat. **21**, 325 (2014).
[29] T. Warwick, Y.-D. Chuang, D. L. Voronov, and H. Padmore, J. Synchrotron Radiat. **21**, 736 (2014).
[30] T. Hatsui, H. Setoyama, E. Shigemasa, and N. Kosugi, J. Electron Spectrosc. Relat. Phenom. **144-147**, 1059 (2005).
[31] H. Yamane, N. Kosugi, and T. Hatsui, J. Electron Spectrosc. Relat. Phenom. **188**, 155 (2013).
[32] J. Nordgren, G. Bray, S. Cramm, R. Nyholm, J.-E. Rubensson, and N. Wassdahl, Rev. Sci. Instrum. **60**, 1690 (1989).
[33] See https://portal.slac.stanford.edu/sites/lcls_public/instruments/SXR/endstations/Pages/ES_MomentumResolved.aspx for LCLS SXR.
[34] M. C. Hettrick and J. H. Underwood, Appl. Opt. **25**, 4228 (1986).
[35] J. A. Samson and D. L. Ederer, *Vacuum Ultraviolet Spectroscopy* (Academic Press, 2000).
[36] C. Bostedt, S. Boutet, D. M. Fritz, Z. Huang, H. J. Lee, H. T. Lemke, A. Robert, W. F. Schlotter, J. J. Turner, and G. J. Williams, Rev. Mod. Phys. **88**, 015007 (2016).
[37] A. S. Tremsin, J. V. Vallerga, J. B. McPhate, and O. H. W. Siegmund, Nucl. Instrum. Methods Phys. Res., Sect. A **787**, 20 (2015).
[38] J. S. Morgan, D. C. Slater, J. G. Timothy, and E. B. Jenkins, Appl. Opt. **28**, 1178 (1989).
[39] K. Amemiya, Y. Kitajima, T. Ohta, and K. Ito, J. Synchrotron Radiat. **3**, 282 (1996).
[40] K. Amemiya and T. Ohta, J. Synchrotron Radiat. **11**, 171 (2004).
[41] F. Cerrina and M. Sanchez del Rio, in *Ray Tracing of X-ray Optical Systems*, Handbook of Optics, 3rd ed., edited by M. Bass (McGraw Hill, New York, 2009), Vol. 5, Chap. 35.
[42] M. Sanchez del Rio, N. Canestrari, F. Jiang, and F. Cerrina, J. Synchrotron Radiat. **18**, 708 (2011).
[43] V. N. Strocov, T. Schmitt, U. Flechsig, L. Patthey, and S. G. Chiuzbăian, J. Synchrotron Radiat. **18**, 134 (2011).
[44] R. Qiao *et al.*, "High-efficiency in-situ Resonant Inelastic X-ray Scattering (iRIXS) Endstation at the Advanced Light Source," Rev. Sci. Instrum. (submitted).
[45] J. M. Tarascon and M. Armand, Nature **414**, 359 (2001).
[46] M. S. Whittingham, Chem. Rev. **104**, 4271 (2004).
[47] Q. Li, R. Qiao, L. A. Wray, J. Chen, Z. Zhuo, Y. Chen, S. Yan, F. Pan, Z. Hussain, and W. Yang, J. Phys. D: Appl. Phys. **49**, 413003 (2016).
[48] K. Luo, M. Roberts, R. Hao, N. Guerrini, D. Pickup, Y.-S. Liu, K. Edström, J.-H. Guo, A. Chadwick, L. Duda, and P. Bruce, Nat. Chem. **8**, 684 (2016).
[49] X. Liu, D. Wang, G. Liu, V. Srinivasan, Z. Liu, Z. Hussain, and W. Yang, Nat. Commun. **4**, 2568 (2013).
[50] J.-H. Guo, J. Electron Spectrosc. Relat. Phenom. **188**, 71 (2013).
[51] T. Ohzuku and Y. Makimura, Chem. Lett. **30**, 642 (2001).
[52] J. A. Bearden, Rev. Mod. Phys. **39**, 78 (1967).
[53] G. Ghiringhelli, M. Matsubara, C. Dallera, F. Fracassi, A. Tagliaferri, N. B. Brookes, A. Kotani, and L. Braicovich, Phys. Rev. B **73**, 035111 (2006).